Tectonophysics 498 (2011) 27–34

Contents lists available at ScienceDirect

Tectonophysics

journal homepage: www.elsevier.com/locate/tecto

Upper mantle seismic velocity anomaly beneath southern Taiwan as revealed by teleseismic relative arrival times

Po-Fei Chen [a,*], Bor-Shouh Huang [b], Ling-Yun Chiao [c]

[a] Institute of Geophysics, National Central University, Taiwan
[b] Institute of Earth Sciences, Academia Sinica, Taiwan
[c] Institute of Oceanography, National Taiwan University, Taiwan

ARTICLE INFO

Article history:
Received 29 March 2010
Received in revised form 22 November 2010
Accepted 24 November 2010
Available online 28 November 2010

Keywords:
Taiwan tectonics
Teleseismic relative arrival times
Genetic algorithm
Fast marching method
Pseudospectral method

ABSTRACT

Probing the lateral heterogeneity of the upper mantle seismic velocity structure beneath southern and central Taiwan is critical to understanding the local tectonics and orogeny. A linear broadband array that transects southern Taiwan, together with carefully selected teleseismic sources with the right azimuth provides useful constraints. They are capable of differentiating the lateral heterogeneity along the profile with systematic coverage of ray paths. We implement a scheme based on the genetic algorithm to simultaneously determine the relative delayed times of the teleseismic first arrivals of array data. The resulting patterns of the delayed times systematically vary as a function of the incident angle. Ray tracing attributes the observed variations to a high velocity anomaly dipping east in the mantle beneath the southeast of Taiwan. Combining the ray tracing analysis and a pseudo-spectral method to solve the 2-D wave propagations, we determine the extent of the anomaly that best fits the observations via the forward grid search. The east-dipping fast anomaly in the upper mantle beneath the southeast of Taiwan agrees with the results from several previous studies and indicates that the nature of the local ongoing arc–continent collision is likely characterized by the thin-skinned style.

1. Introduction

Taiwan sits atop the convergent boundary between the Eurasia Plate (EUP) and the Philippine Sea Plate (PSP). The subduction that occurs as a result of the 7–8 cm/yr convergence rates flips the polarity in the vicinity of Taiwan. To the south, the South China Sea portion of the EUP is subducting to the east, underneath the PSP along the Manila Trench. To the north, the predominantly northwest-dipping PSP slab subducts underneath the EUP along the Ryukyu Trench. The pivot of the transition, Taiwan, has been undergoing arc–continent collision since at least 4 m.a. (Ho, 1986), resulting in both rapid uplifting rate and thus modern high mountain ranges and frequent, devastating earthquakes, e.g., the 1999 Mw 7.0 Chi-Chi earthquake. The collision is oblique to the plate boundary and propagates southwesterly. Temporal evolution of the orogenic processes can thus be envisioned by a series of co-latitudinal slices northward from the offshore region of southern Taiwan. They include the east-dipping EUP subduction, in which oceanic lithosphere is consumed off the shore of southern Taiwan, an incipient collision between the EUP continental shelf and the PSP Luzon arc in southern Taiwan, a progressive full-scale collision of the topographic high in central Taiwan, and the post-collision relaxation and flipping of the subduction polarity in northern Taiwan.

Tectonic and geological manifestations of the collisional orogeny have been documented for decades. The nature of the detailed mechanisms of the collision, however, is still under debate. The major argument focuses on the depth scale of the EUP involved in the collision. Whereas the thin-skinned model involves only the crustal part of the EUP (Suppe, 1981), the entire lithosphere of the EUP is proposed to collide with the PSP in the thick-skinned model (Wu et al., 1997). The thin-skinned collision is based on the scenario of subduction and thus implicitly assumes that the east-dipping EUP extends northward all the way to central Taiwan, despite the northern termination of the Manila Trench offshore to the southwestern Taiwan. On the other hand, the thick-skinned collision in central Taiwan bears little connection with an east-dipping EUP to the south. The resolution of the debate thus depends on the verification of the presence or the absence of an east-dipping slab beneath central and southern Taiwan. Being able to clarify the style of the collision also helps distinguish the proposed models for the orogeny. For instance, for the orogenic mechanism of crustal exhumation (Lin, 2002) to be sustained, the style of the collision must be thin-skinned.

Several distinct methods have been used to examine whether or not the east-dipping EUP off the shore of southern Taiwan extends to central Taiwan. For example, the travel-time residuals and amplitude differences of teleseismic P arrivals, as observed by the Broadband Array in Taiwan for Seismology (BATS), have been investigated (Chen et al., 2004). A dense linear array in central Taiwan was deployed across the suture zone between August and October 2003 to study the

* Corresponding author. Tel.: +886 3 4227151 65647.
E-mail address: bob@ncu.edu.tw (P.-F. Chen).

0040-1951/$ – see front matter © 2010 Elsevier B.V. All rights reserved.
doi:10.1016/j.tecto.2010.11.013

deep crust and mantle structures beneath eastern Taiwan (Lin, 2009). More recently, with a joint inversion of a large number of arrival-time data from local and teleseismic events, a high-resolution 3-D P-wave velocity structure was determined for the crust and upper mantle beneath Taiwan (Wang et al., 2009).

In this study, we use the data collected from a linear broadband array that has been deployed since April 2005. The array transects southern Taiwan in the east–west direction, with 25 stations evenly spaced over a distance of about 140 km (Huang et al., 2006). We carefully picked sizeable teleseismic earthquakes, with epicentral distance ranging from 40° to 80°, in the same azimuth with the linear array (e.g., events from the New Britain Region, the Vanautu Islands and the Fuji Tonga Islands; Fig. 1). In addition, large earthquakes near the antipode from the Nazca subduction zone are also included (Fig. 1). Incident rays of the earthquakes from these subduction zones are on nearly the same cross-sectional plane as the linear array, which provides good teleseismic illumination with a variety of ray angles. In this study, we employed a genetic algorithm to simultaneously align the first P arrivals of the teleseismic events among all stations of the linear array. The resulting patterns of the delayed times systematically vary as a function of the incident angle. Ray tracing attributes the observed variations to a high velocity anomaly dipping east in the mantle SE of Taiwan. Quantitative assessment on the extent and location of the anomaly is further conducted using simulations of the 2-D wave propagations.

2. Methods

2.1. Determining relative arrival times using the genetic algorithm (GA)

Several methods have been proposed for determining the relative delay times of teleseismic body waves within a regional array. One popular method is based on the multi-channel cross correlation (MCCC; VanDecar and Crosson, 1990). MCCC assumes that the errors in the cross-correlation-derived delay times among pairs of many stations are random in nature, and thus, the optimal delay time for each station can be determined by minimizing their overall discrepancies in a least-square sense, a common linear inverse problem (Menke, 1984). However, for noise-contaminated data, the problem is more appropriately posed as non-linear in nature (Rothman, 1985). Both the adaptive stacking method (Rawlinson and Kennett, 2004) and optimization by simulated annealing (Chevrot, 2002) have been proposed to cope with this non-linear inversion. Both methods construct the cost function by measuring the total sum of misfits between the observed traces and the reference trace. The adaptive stacking method derives the reference trace by stacking all of the observed traces with updated time shifts, whereas the simulated annealing solves not only the time shifts of the observed traces but also the amplitude values at each time sample for the reference trace.

Compared with the schemes described above, GA is an even more straightforward method. GA searches for the optimal solution of a non-linear problem by evolving through generations. GA progressively matches the best solution by passing favored characteristics of the current generation of solutions to the next generation. These characteristics are such that they yield the fitness, or the cost function, value toward being optimized (Holland, 1975). One such application is to invoke GA to retrieve the single-crystal constant, C_{ij}, from Brillouin spectroscopy measurements (Chen et al., 2006). In this study, we experiment with GA to simultaneously determine the relative delayed times of teleseismic first arrivals for array data. We first calculate the cross-correlation functions for each pair of traces by the following equation:

$$\phi_{ij}\left(\tau_i,\tau_j\right)=\frac{\sum_{k=1}^{T/\Delta t}\left(x_i k\Delta t+\tau_i\right)x_j\left(k\Delta t+\tau_j\right)}{\sqrt{\sum_{k=1}^{T/\Delta t}x_i^2\left(k\Delta t+\tau_i\right)}\sqrt{\sum_{k=1}^{T/\Delta t}x_j^2\left(k\Delta t+\tau_j\right)}},\qquad(1)$$

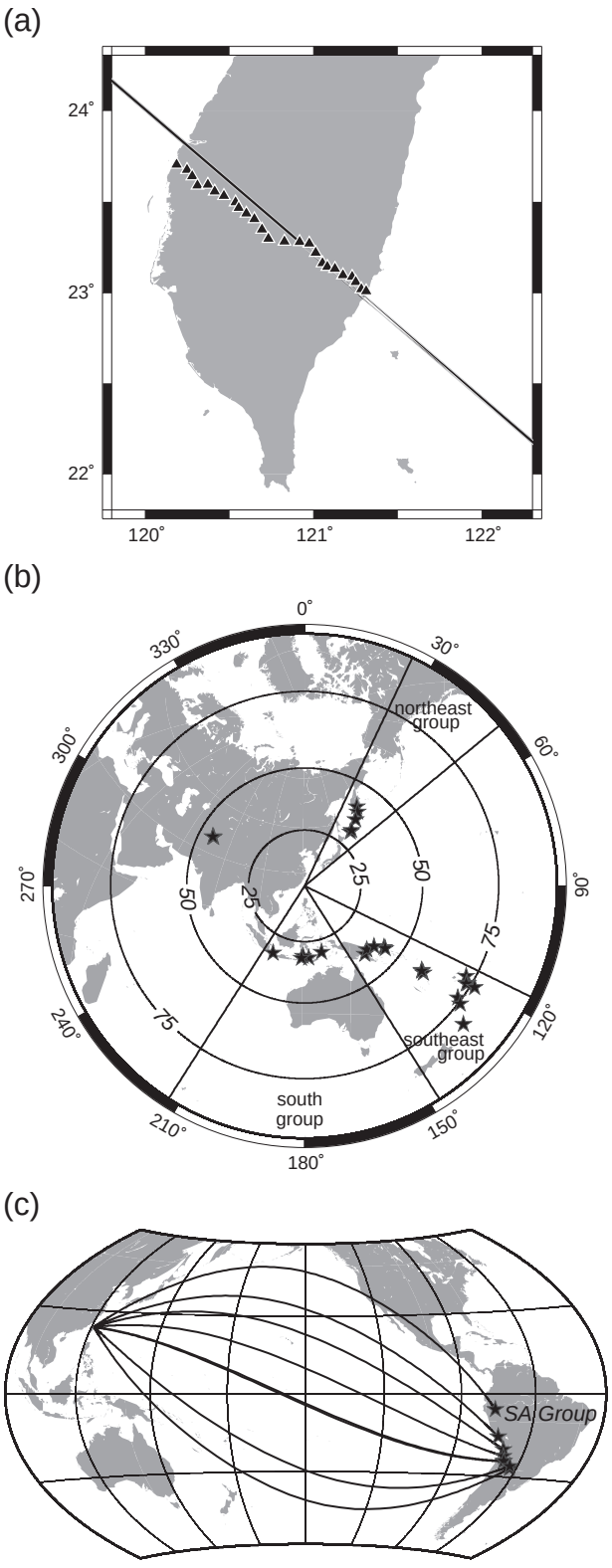

Fig. 1. (a) Distribution of the linear broadband array across southern Taiwan. The line indicates the back azimuth of an earthquake in the southeast group. This line is parallel to the array azimuth. (b) Distribution of earthquakes (stars) with high S/N ratios. According to the back azimuth, they are categorized into groups, and the group names are indicated. (c) Distribution of earthquakes for the SA group and their great circle paths. Note that the epicentral distance is near antipodal.

where T is the length of selected time window, $\Delta t$is the sampling interval, x_i is the ith-trace digital data, and τ_i is the time shift for the ith trace. The same conventions apply to index j for the jth trace. The cost

function is constructed by summing all of the pairs of cross-correlation functions and taking the reciprocal of this sum, as the following

$$C = \frac{1}{\sum_{i=1}^{N}\sum_{j=i+1}^{N}\left|\phi_{ij}\left(\tau_i,\tau_j\right)\right|} + \sum_{i=1}^{N}\left(\tau_i^2\right)^{\frac{1}{2}}, \quad (2)$$

where N is the total number of traces in one earthquake. The second term on the right side ensures that the solutions found are the minimum norm solutions. This approach can thus be considered as a non-linear version of the MCCC method.

We set the initial population size of GA to 300 and ran the algorithm up to 3000 generations to determine the optimal τ_i values that minimize the cost function. The uncertainty of τ_i is estimated by inspecting the cost–function curvature around the optimal τ_i with the other parameters fixed on their optimal values. The error bar is determined by defining an interval in which the cost function is below a given threshold. In retrospect, the alignment method adopted in this study might not be crucial because we only use data with high signal-to-noise ratios and focus on the long wavelength part of the signals (0.1–0.2 Hz).

2.2. Interpreting observations using the ray tracing method

Because the observed delayed-time patterns vary as a function of the incident angle, three earthquakes were selected to represent typical epicentral distances of events around 40°, 70°, and 170°. We employ a fast marching method (FMM; Rawlison et al., 2006) to trace the 3-D ray paths. FMM is a grid-based scheme to solve the eikonal equation. For initialization of the teleseismic wavefronts, the paths from distant sources to the boundary of interests were first carried out using a global reference model (Rawlison et al., 2006). We are interested in the part of the crust and the upper mantle beneath the receiving array. The traced 3-D ray paths in the region were projected onto the cross-sectional plane of the linear array. This 2-D approximation is valid because all of the earthquakes were located along the azimuth of the linear array. We then marked paths with anomalous relative arrival times and interpret the preliminary result qualitatively.

2.3. Determining the extent of the velocity anomaly using 2-D wave propagation

To fully use the magnitudes of the delayed times and to put the full wave field into consideration, we used a pseudospectral method to simulate the two-dimensional plane wave propagations. This method uses fast Fourier transforms to compute the spatial derivative of the wave equations and the second-order differentiating approximation to calculate the marching time (Huang, 1992). Without losing generality, we invoke the simplification in solving the antiplane problem. The plane wave propagations were simulated to mimic those of the three representative earthquakes. The period of the wave was set between 5 and 10 s and corresponds to the 0.1–0.2 Hz frequency band of observation. A virtual array was set up to have the same distribution as the real stations that record the propagating waves. The synthetic arrival-time patterns of the virtual stations were derived by subtracting the relative arrival times of the reference computation from those of the anomaly computation. The reference computation uses a 1-D global velocity model, and the anomaly computation is carried out by superimposing a body of fast velocity anomaly – with probable features determined by results of ray tracing – on the original 1-D model. The relative arrival times of both of the computations were obtained by the MCCC method. Finally, the adequate parameters that control the anomalous structure were determined by a straightforward grid search.

3. Data and processing

Teleseismic earthquakes between May 2005 and December 2007 were selected from the Global CMT catalogue (Ekström et al., 2005). Those with epicentral distances greater than 25°, depths deeper than 70 km, and clear first P arrivals were sorted out for analyzing. We categorized the events into four groups according to their back-azimuth distributions. These groups were the South America (SA) group, the southeast group, the south group, and the northeast group (Fig. 1). The SA and southeast groups constitute the unique source–receiver geometry mentioned earlier, and only the results for these two groups were discussed.

Vertical components of the array data were filtered with a bandpass between 0.1 and 0.2 Hz. The sampling rate of the array data was 20 points per second. We calibrated with respect to the theoretical travel time that was calculated by the ak135 (Kennett et al., 1995) global reference model. A referenced time of 100 s was set as the predicted time of the corrected first arrivals (Fig. 2). For earthquakes in the SA group, the first arrival was the PKPdf phase. A proper time window was cut manually to ensure the inclusion of the target phase. We have observed that a time window of 20–40 s is more than sufficient to include the 0.1–0.2 Hz first arrivals. Data within this time window were then processed with GA to determine the relative arrival times. In most cases, GA was able to align the target phase for all traces because those data have clear first arrivals (Fig. 3). However, a more stringent standard was adopted in that we only kept data for which the target phase was aligned and exhibited an obvious level of waveform similarities. The width of the estimated error bar is shown in Fig. 4.

4. Results

4.1. Patterns of relative arrival times

We projected stations onto the 2-D cross-sectional plane of the linear array and find three key observations (Figs. 5 and 6). That is: (1) Earthquakes with similar epicentral distances exhibit similar delayed-time patterns, suggesting that the observations are robust and deserve interpretations. (2) A positive travel time residual is consistently present at a single station located at a distance around 127 km, implying an *in situ* shallow structure with a low velocity anomaly. The causes of

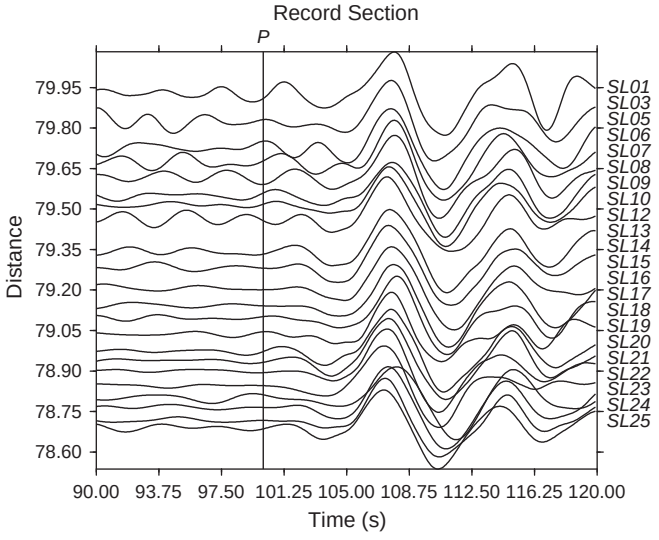

Fig. 2. First P of a Fuji–Tonga earthquake with the theoretical first arrival setting at 100 s referenced time (the vertical thick line). Each trace is normalized. The station names are given on the right.

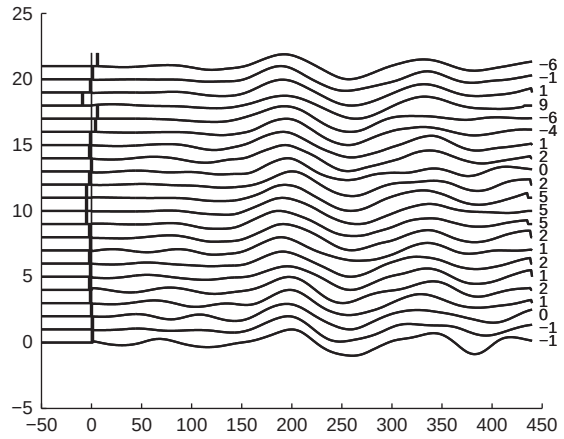

Fig. 3. The alignment of the first arrivals by GA. The thick vertical bars indicate amount of shifting for the corresponding trace with numbers to the right showing shifting points. The sampling rate is 20 points per second.

the short wavelength variation remain unclear to us. Because our goal was to investigate the upper mantle velocity structure, observations from this particular station were discarded. (3) The long wavelength patterns for the delayed times exhibit a systematic variation as a function of the incident angle. The overall slopes increase with decreasing epicentral distances (Figs. 5 and 6) and we can group the entire linear array into three subregions. The delay times of each subregion can be roughly approximated by the average of the delayed times from stations within the region. The three subregions from left to right are the Western Plain (WP), the Central Mountain (CM), and the Coastal Range (CR). The systematic variation of the delayed-time patterns can be described by the differential delayed times, $CR_{\text{delayed times}} - WP_{\text{delayed times}}$. These times measured at ~−1, 0, and ~1 s, corresponding to epicentral distances of ~170°, ~80°, and ~40°, respectively (Figs. 5 and 6).

4.2. Interpreting observations based on results of ray tracing

The projected rays of the three representative earthquakes (epicentral distances at 170°, 79°, and 43°) are shown in Fig. 7, and the fast paths are marked with thick lines. We use an ellipse (marked A) to mark the area of the fast-path intersection for the 170° and 43° earthquakes. Ellipse A indicates an area where a fast velocity anomaly will induce negative delayed times in the CR stations for the 170° earthquake and in the WP stations for the 43° earthquake. This area complies with the opposite delayed-time patterns of the two representative earthquakes. To further explain the nearly flat pattern of the 79° earthquake, the paths

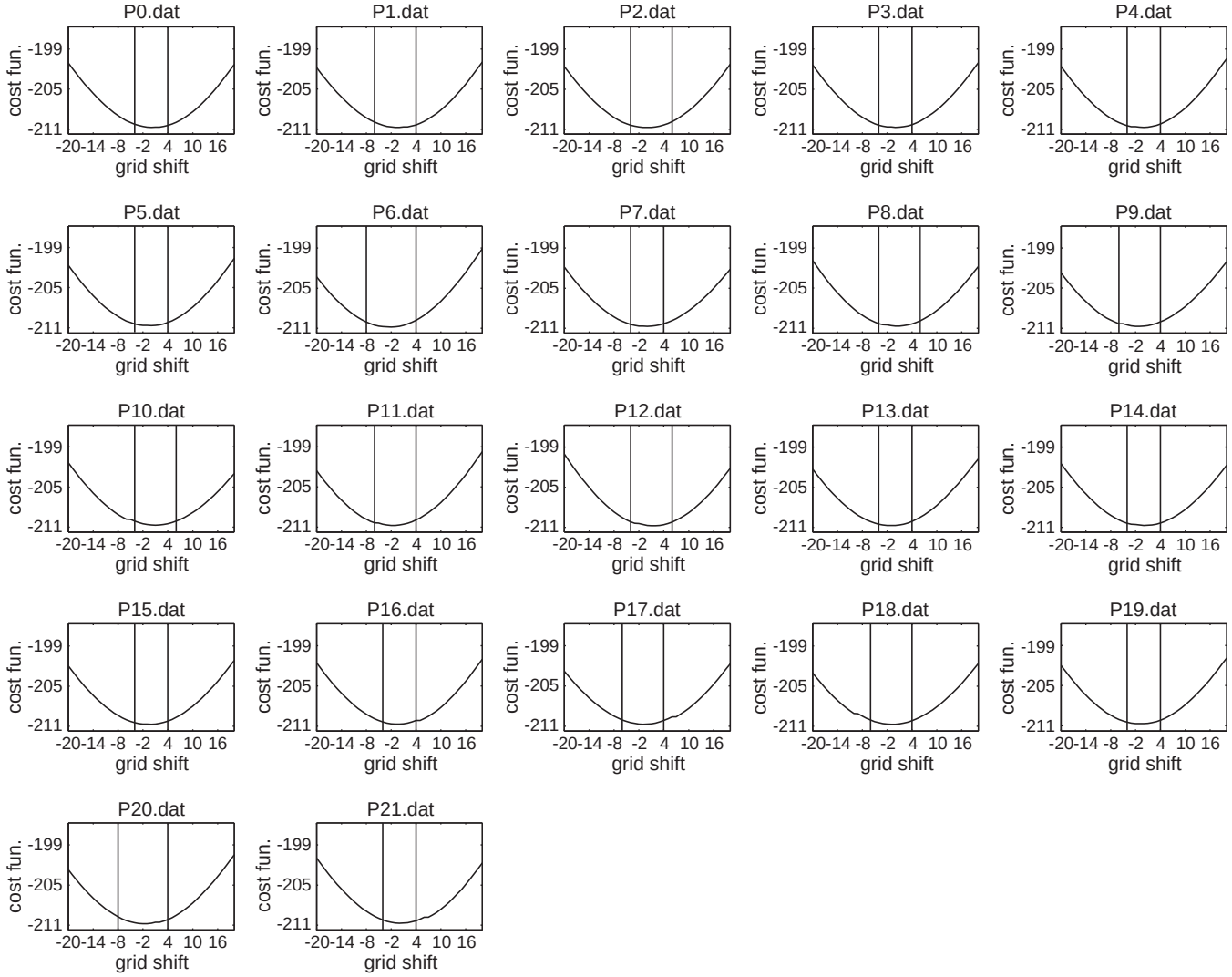

Fig. 4. Curvatures of the cost function for each station near its optimal delay time. The error bar is determined by defining an interval in which the cost function is or below a certain threshold (the vertical lines).

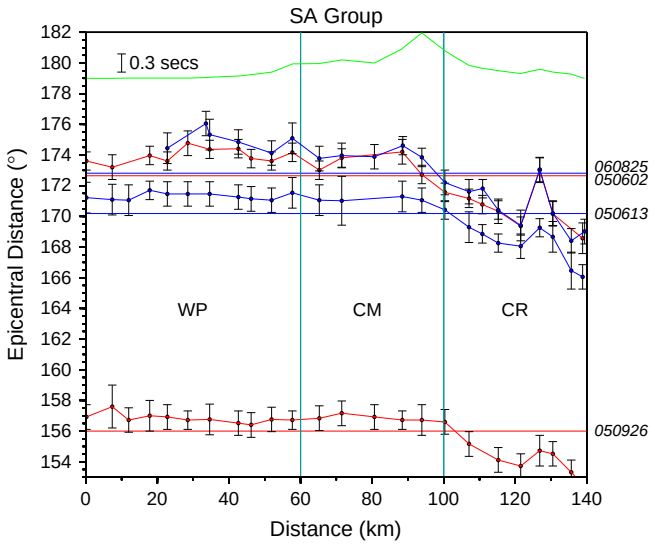

Fig. 5. Patterns of the relative arrival times for earthquakes in the SA group. The distance is measured relative to the left-most station on the cross-sectional plane of the array. For each earthquake, a horizontal line representing the mean arrival time is plotted at the y coordinate proportional to its epicentral distance. The magnitudes of the delayed time for each station are plotted as vertical shifts from the horizontal line with a scaled bar indicated to the upper left. The green line shows the back ground topography. The year, month, and day of the earthquakes in yymmdd format is indicated on right. WP stands for the Western Plain, CM for the Central Mountain Range, and CR for the Coastal Range. Note the consistent pattern of the relative arrival times for earthquakes in the SA group.

of which are marked by thick lines, a larger ellipse (marked B) must be used. To exclude the slow paths (thin lines) of the other two events, Ellipse B dips somewhat to the southeast (Fig. 7).

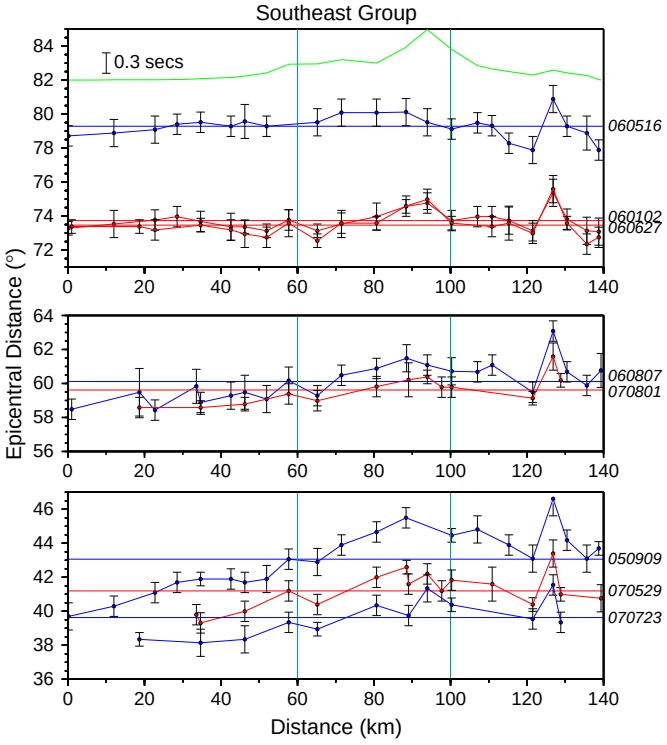

Fig. 6. This figure is the same as Fig. 5, but the earthquakes are in the southeast group. Note the similar pattern of the relative arrival times for the earthquakes that have similar epicentral distances. The pattern systematically varies as a function of the epicentral distance.

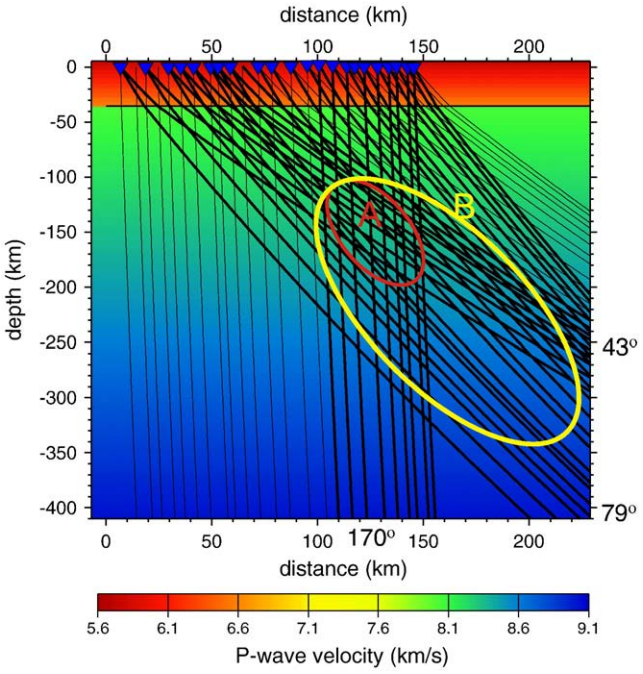

Fig. 7. The ray paths of three representative earthquakes with epicentral distances at 43°, 79°, and 179° projected onto the cross-sectional plane of the array. Blue reversed triangles are the locations of the stations. For each earthquake, the ray paths to the stations with relatively negative travel times are drawn as thick lines, indicating relatively fast paths. All of the ray paths of the 79° earthquake are thick lines. This earthquake has a nearly flat pattern of relative arrival times. A fast anomaly at the red circle (marked A) explains the earthquakes at 43° and 170°. However, to include the 79° earthquake, the anomaly must spread deeper to the southeast as indicated by the yellow circle (marked B). The distance refers to the left-most station.

4.3. Determining the extent of the velocity anomaly using 2-D wave propagations

The results of the ray-tracing study show that the center of the fast anomaly is ~250 km from the left-most station and has a probable depth range between 150 and 250 km. This anomaly has an elliptical shape with significant dipping angles, which are 75° roughly to the southeast. We assume that the spatial variations of the velocities follow a Gaussian distribution along both axes of the ellipse. The observations of the three representative earthquakes were smoothed with a 5-point average to eliminate the short-wavelength undulations. Fig. 8 shows the propagations of the 2-D plane wave with an incident angle that imitates the incident plane waves of the 43° earthquake. Three trial runs were conducted with center depths at 150, 200, and 250 km to determine the optimal values of the following three parameters: (1) the variances along the long and (2) the short axis of the anomalous ellipse and (3) the maximum velocity anomalies at the center. This determination is based on a grid search within a 3-D space that is within the probable ranges of the three parameters. The third trial run, which had center depths at 250 km, provided the solution that best fits the smoothed data. The maximum velocity anomaly at the center is ~12% faster than the reference model. The optimal variance is ~50 km along the SE dipping axis and ~20 km along the SW dipping axis (Fig. 9). Comparisons between the observed delayed times (smoothed) and the simulated times are shown in Fig. 10, where the long wavelength features of the observations are mostly comparable to the long wavelength features of simulated results.

5. Discussion

The application of GA to simultaneously determine the delayed times of teleseismic P from array data by formulating the non-linear

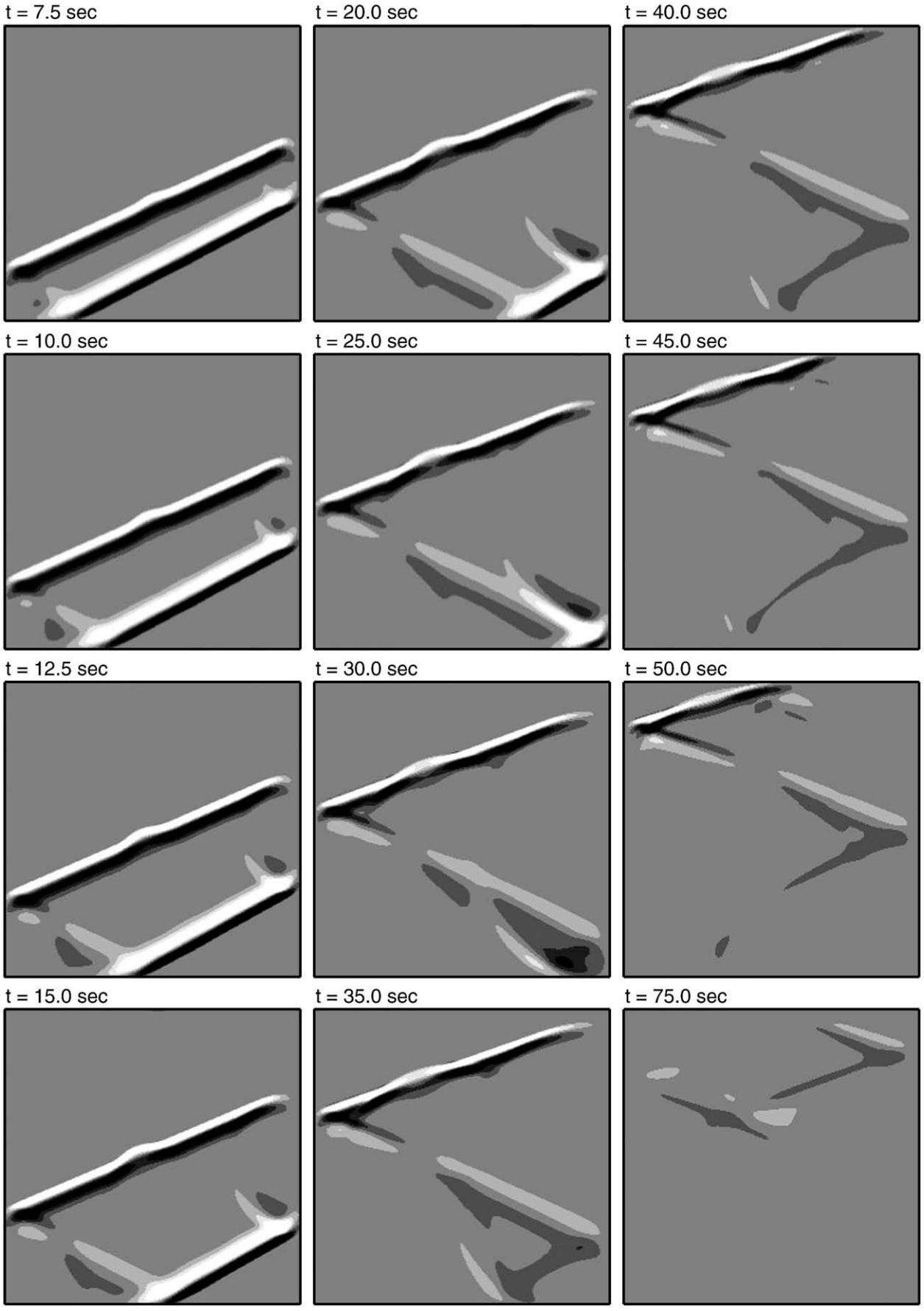

Fig. 8. Propagations of a 2-D plane wave with an incident angle that imitated that of an earthquake at a 43° epicentral distance. Note the effects of a fast velocity anomaly near the middle of the simulation domain starting at 10 s. The later phase is an artificial effect of the boundary condition.

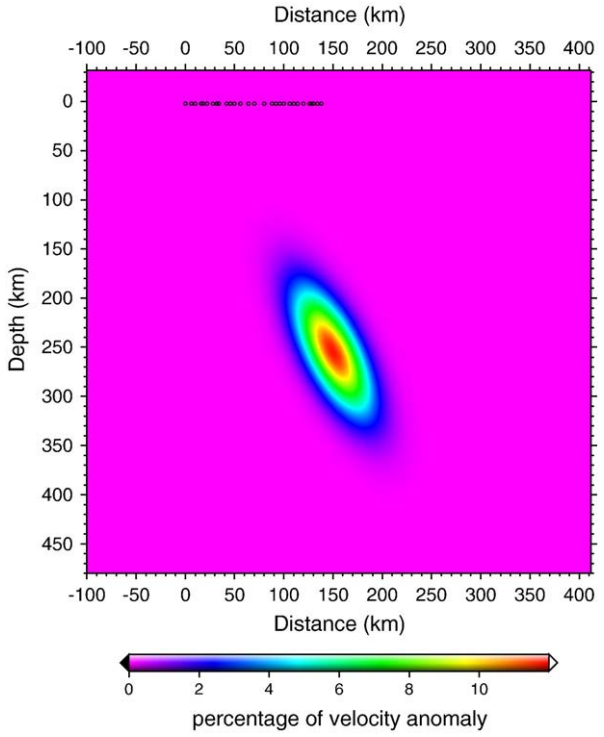

Fig. 9. The size and magnitude of the fast anomalies that best fits the observations. The ellipse center is at 250 km. The line of small circles on the top is the virtual array that corresponds to the locations of true stations. The reference point is the left-most station.

fitness based on cross correlation was quite satisfactory. Although GA is a nearly global domain search scheme that locates the optimal solution at the expense of computer time, the distinction between the GA used in this study and MCCC is minor in terms of the alignment results, because of the high S/N ratio of the data used in this study. We suspect that all of the methods mentioned earlier (e.g., adaptive stacking and simulated annealing) may work equally well for the purpose of this study based on high quality data, and some of them may be even more efficient than GA. Further assessment should probably compare GA with MCCC on a data set with low S/N ratios.

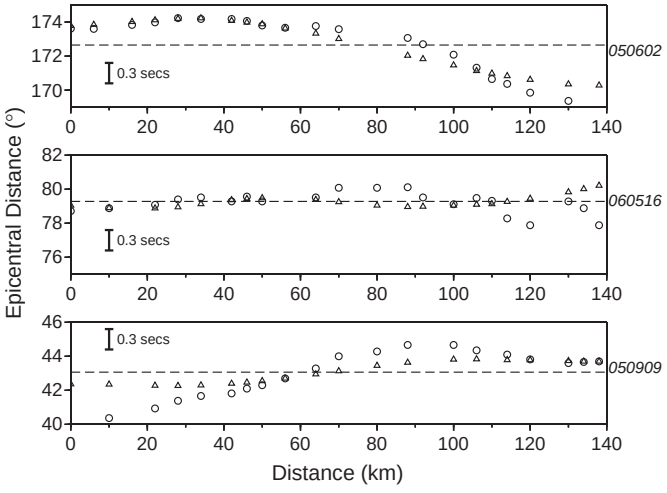

Fig. 10. Comparison of observations and simulations of the three representative earthquakes. The circles are smoothed observations of the relative arrival times. The triangles are the relative arrival times that were simulated using the anomaly shown in Fig. 9. The format of this figure is the same as in Fig. 5. The long wavelength features of the observations are exhibited mostly by the simulations, but the fitting could be improved in the future.

The delayed-time patterns are attributed to both crustal and upper mantle heterogeneities. We argue that the upper mantle is the main contributor for the following reasons: (1) We deliberately used 0.1–0.2 Hz bandpass signals, which correspond to tens of kilometers of wavelength. The long wavelength signal is suitable for detecting velocity anomalies of a similar scale. The observed variation pattern reveals the existence of a fast anomaly in the upper mantle; (2) The delayed times mainly exhibit a long wavelength pattern in space. The pattern is most likely associated with a deep origin. The deep origin is further confirmed by the fact that, among the tested depths (150, 200, and 250 km) of the ellipse center, the minimum misfit solution occurred at the deepest level (250 km); (3) The variation pattern between the earthquakes most likely implies the upper mantle heterogeneities because the crustal effects are similar regardless of the incident angles; (4) The results of the ray tracing suggest that an anomaly cannot be inserted exclusively into the crust to reconcile the observations.

Because of the scarcity of ray coverage, no tomographic studies that map the high resolution deep velocity structure beneath southern Taiwan are presently available. Our forward grid search approach quantitatively constrains the extent of the anomalous structure. The synthetic patterns of relative arrival times basically summarize the long-wavelength feature of the observations (Fig. 10). The resulting feature of the velocity anomaly derived in this study is consistent with slab signature. Although the ~12% fast anomaly at the center is high compared to global tomography studies (Li and van der Hilst, 2010), that value can be amended if we can improve our constraints on the spatial distribution of the anomaly in the future.

Results of this study are consistent with those from previous studies. The reduced travel times and amplitudes of the teleseismic P form the Tonga–Kermadec earthquakes in central Taiwan stations have been interpreted as a result of an east-dipping cold anomaly in the upper mantle (Chen et al., 2004). Right above our high velocity anomaly, which is at depths around 89 km, is an east-dipping EUP slab that was identified by observations of a phase that originated from an intermediate-depth earthquake off the shore of southeastern Taiwan and refracted from its Moho-discontinuity. This study used a dense linear array in central Taiwan deployed across the suture zone (Lin, 2009). Our 2-D image (Fig. 9) corresponds to the L2–L3 vertical cross-section in Fig. 14 of the tomographic study of Wang et al. (2009). Results of both studies consistently exhibit the prominent feature of an east-dipping cold anomaly in the upper mantle beneath SE Taiwan. However, the results differ in the position, magnitude, and extent of the anomaly. The center of the high velocity anomaly in this study is tens of kilometers deeper and a few percentages higher than that of Wang et al. (2009). The spatial distribution of the high anomaly is comparable in both studies at depths below 100 km but different above 100 km. These discrepancies might be attributed to the fact that in this study we used relative long wavelength signals, neglected crustal effects, and presumed a simplified geometry for the anomaly. Furthermore, in the study of joint inversion, the degrees of validation of invoking ray theory are different for local and teleseismic events.

Although the 2-D teleseismic illumination of this study is limited in a cross-sectional view compared to other more comprehensive studies (Chen et al., 2004; Lin, 2009; Wang et al., 2009), the results agree with other studies that an east-dipping high anomaly slab exits in the upper mantle beneath SE Taiwan. This study provides an independent constraint on the existence of the discussed slab. The compliance supports the conclusions drawn by other studies (Chen et al., 2004; Lin, 2009; Wang et al., 2009) suggesting that the east-dipping EUP extends to central Taiwan. The extension of the slab in the upper mantle beneath southern and central Taiwan implies that the tectonic environment preceded collision in central Taiwan was most likely a subduction system and that the nature of the collision was of the thin-skinned style. The absence of deep seismicity might be attributed to the exhaustion of the oceanic lithosphere and thus lacking of hydrous minerals (Chen et al., 2004).

In the framework of Wilson cycle for supercontinents formation, the consumption of oceanic lithosphere through subduction along passive continental margin is a necessary preceding stage for the suture of two continents. It is a natural consequence that the continent collides with the subduction-formed arc when the oceanic lithosphere attached to the passive margin is completely consumed. The arc–continent collision is currently widely accepted driving force for Taiwan orogeny (Teng, 1990). Therefore, the observed fast anomaly in the upper mantle beneath central and southern Taiwan might be interpreted as the remains of preceding subducting slab. To rewind one time step, the flipping of subduction to the north of Taiwan sets the stage to consume the oceanic lithosphere on the other side of convergent boundary, which is dynamically plausible if the slab remains are detached due to negative buoyancy. In summary, the observation of this study fits the tectonics of Taiwan into a greater picture of Wilson cycle. What is unique here is that the evolution through time is well presented over a relatively short distance from south to north. It is thus feasible to understand the essential process of Wilson cycle by studying the tectonics of Taiwan.

6. Conclusions

The application of GA to simultaneously determine the delayed times of teleseismic P within the linear array was successful for the high S/N ratio data used in this study. Further research is needed to compare GA with MCCC for data with a low S/N ratio. The long-wavelength delayed-time patterns of the teleseismic P along the linear array that transects southern Taiwan systematically varies with the incident angle. By using ray tracing, the observed variations can be attributed to a high velocity anomaly in the mantle SE of Taiwan. This anomaly likely has an east-dipping geometry. Using results of ray tracing and employing a pseudospectral method to simulate 2-D wave propagations, we quantitatively determined the simple geometry of the anomaly catching long-wavelength features of the observations via a straightforward grid search. An east-dipping high velocity anomaly in the upper mantle beneath SE Taiwan agrees with the results of other studies and it is the remains of preceding subducting slab, which suggests that the style of the collision was thin-skinned.

Acknowledgements

We acknowledge the reviewer and the Editor for their suggestions that significantly improve the manuscript. This work was supported by the Taiwan Earthquake Research Center (TEC) funded through National Science Council (NSC) with grant number 98-2116-M-008-019. The TEC contribution number for this article is 0074.

References

Chen, P.-F., Huang, B.-S., Liang, W.-T., 2004. Evidence of a slab of subducted lithosphere beneath central Taiwan from seismic waveforms and travel times. Earth Planet. Sci. Lett. 229, 61–71.
Chen, P.-F., Chiao, L.-Y., Huang, P., Yang, Y., Liu, L., 2006. Elasticity of magnesite and dolomite from a genetic algorithm for inverting Brillouin spectroscopy measurements. Phys. Earth Planet. Inter. 155, 73–86. doi:10.1016/j.pepi.2005.10.004.
Chevrot, S., 2002. Optimal measurement of relative and absolute delay times by simulated annealing. Geophys. J. Int. 151, 164–171.
Ekström, G., Dziewonski, A.M., Maternovkaya, N.N., Nettles, M., 2005. Global seismicity of 2003: centroid-moment-tensor solutions for 1087 earthquakes. Phys. Earth Planet. Inter. 148 (1–2), 327–351.
Ho, C.S., 1986. A synthesis of the geologic evolution of Taiwan. Tectonophysics 125, 1–16.
Holland, J., 1975. Adaptation in Natural and Artificial Systems. The University of Michigan Press, Ann Arbor.
Huang, B.-S., 1992. A program for two-dimensional seismic wave propagation by the pseudospectrum method. Comput. Geosci. 18, 289–307.
Huang, B.-S., Huang, W.-G., Liang, W.-T., Rau, R.-J., Hirata, N., 2006. Anisotropy beneath an active collision orogen of Taiwan: results from across islands array observations. Geophys. Res. Lett. 33, L24302. doi:10.1029/2006GL027844.
Kennett, B.L.N., Engdahl, E.R., Buland, R., 1995. Constraints on seismic velocities in the Earth from travel times. Geophys. J. Int. 122, 108–124.
Li, C., van der Hilst, R.D., 2010. Structure of the upper mantle and transition zone beneath Southeast Asia from traveltime tomography. J. Geophys. Res. 115, B07308. doi:10.1029/2009JB006882.
Lin, C.-H., 2002. Active continental subduction and exhumation: the Taiwan orogeny. Terra Nova 14 (No. 4), 281–287.
Lin, C.-H., 2009. Compelling evidence of an aseismic slab beneath central Taiwan from a dense linear seismic array. Tectonophysics 466, 205–212.
Menke, H., 1984. Geophysical Data Analysis: Discrete Inverse Theory. Academic Press, Orlando, Florida.
Rawlinson, N., Kennett, B.L.N., 2004. Rapid estimation of relative and absolute delay times across a network by adaptive stacking. Geophys. J. Int. 157, 332–340.
Rawlison, N., de Kool, M., Sambridge, M., 2006. Seismic wavefront tracking in 3D heterogeneous media: applications with multiple data classes. Explor. Geophys. 37, 322–330.
Rothman, D.H., 1985. Nonlinear inversion, statistical mechanics, and residual statics estimation. Geophysics 50, 2784–2796.
Suppe, J., 1981. Mechanics of mountain building and metamorphism in Taiwan. Geol. Soc. China. 4, 67–89.
Teng, L.S., 1990. Geotectonic evolution of Late Cenozoic arc–continent collision in Taiwan. Tectonophysics 183, 57–76.
VanDecar, J.C., Crosson, R.S., 1990. Determination of teleseismic relative arrival times using multi-channel cross-corelation and least squares. Bull. Seismol. Soc. Am. 80, 150–169.
Wang, Z., Fukao, Y., Zhao, D., Kodaira, S., Mishra, O.P., Yamada, A., 2009. Structural heterogeneities in the crust and upper mantle beneath Taiwan. Tectonophysics 476, 460–477. doi:10.1016/j.tecto.2009.07.018.
Wu, F.T., Rao, R.J., Salzberg, D., 1997. Taiwan orgeny: thin-skinned or lithospheric collision? Tectonophysics 274, 191–220.